FIGURE 2-14 A through-focus series of images of a portion of a fly's eye. Each optical section was recorded in real time using standard nonlaser illumination.
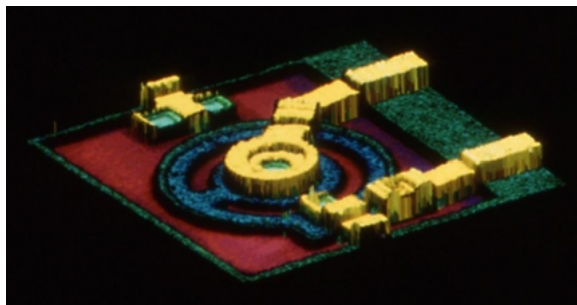

FIGURE 2-16 A computer-generated false-color image of a portion of a transistor. The color represents surface height and the depth range from pale yellow to blue is 6 mm.
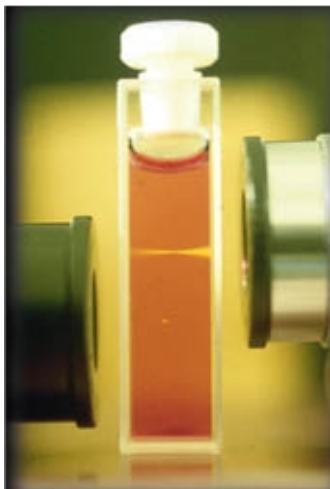
FIGURE 3-8 Spatial extension of the fluorescence emission from a solution containing fluorescent molecules under one- and two-photon excitation. In the case of TEP, the excitation phenomenon, small spots in the lower part of the cuvette, takes place only within a diffraction-limited volume. This volume can be roughly quantified using the resolution parameters of the system. In the case of conventional or one-photon excitation, the double-cone geometry (the upper bright area in the cuvette) is evident. The main implications of this behavior are an inherent confocal effect and consequent optical sectioning property, and photobleaching and phototoxicity confined to a sub-femtoliter volume. (Picture courtesy of John Girkin from Biorad web homepage.)
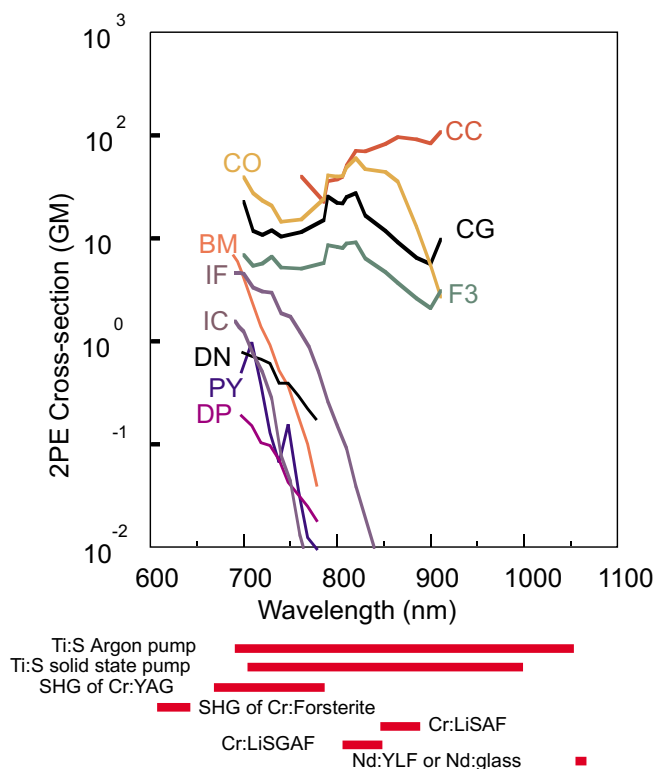
FIGURE 4-3 Two-photon fluorescence excitation spectra of fluorophores. For BM, data are for the two-photon absorption cross-sections. For all the other fluorophores, data are for the two-photon action cross-section (i.e., the product of the fluorescence emission quantum efficiency and the two-photon absorption cross-section). $1\,\mathrm{GM} \equiv 10^{-50}\,\mathrm{cm^4\,s/photon}$. Spectra are excited with linearly polarized light using a mode-locked Ti : sapphire laser. For comparison, the tuning ranges of conveniently available mode-locked laser sources are also plotted. The fluorophores illustrated are as follows: BM $\equiv$ *p*-bis(*o*-methylstyryl)benzene; DP (DAPI not DNA-bound) $\equiv$ 4′,6-diamidino-2-phenylindole, dihydrochloride; DN (dansyl) $\equiv$ 5-dimethylaminonaphthalene-1-sulfonylhydrazine; PY $\equiv$ 1,2-bis-(1-pyrenedecanoyl)-*sn*-glycero-3-phosphocholine; IC $\equiv$ indo-1 with Ca^{2+}; IF $\equiv$ indo-1 without Ca^{2+}; CG $\equiv$ calcium green-1 with Ca^{2+}; CO $\equiv$ calcium orange with Ca^{2+}; CC $\equiv$ calcium crimson with Ca^{2+}; F3 $\equiv$ fluo-3 with Ca^{2+}. All of the samples were purchased from either Eastman Kodak or Molecular Probes. Note that the *y* axis is a logarithmic scale.
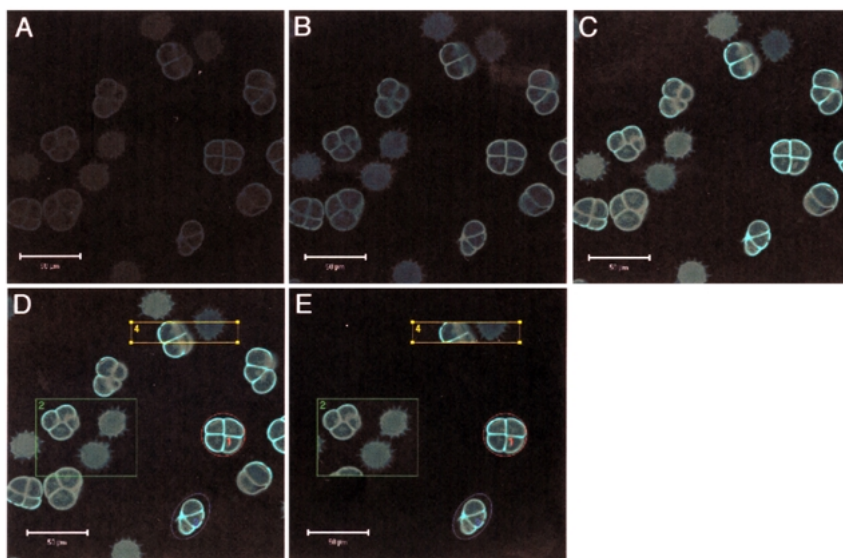
FIGURE 8-12 Using the AOM to modulate the percentage transmission of laser pulses and ROI scanning. (*A*), (*B*), and (*C*) show the same field imaged using 20%, 35% and 56% transmission of the laser pulses. (*D*) and (*E*) illustrate the use of ROI scanning to scan only the regions indicated by the colored rectangles. (M. Dickinson, unpublished observations.)
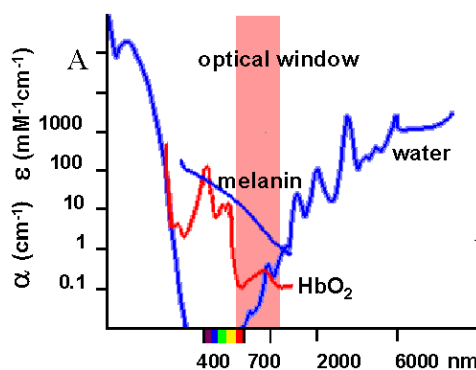

FIGURE 9-1 Absorption spectra of the cellular absorbers water, melanin, and hemoglobin. The range of low absorption and low scattering is from about 600 nm up to 1200 nm (optical window). At higher NIR wavelengths, linear absorption of water increases, and may induce destructive linear heating effects.
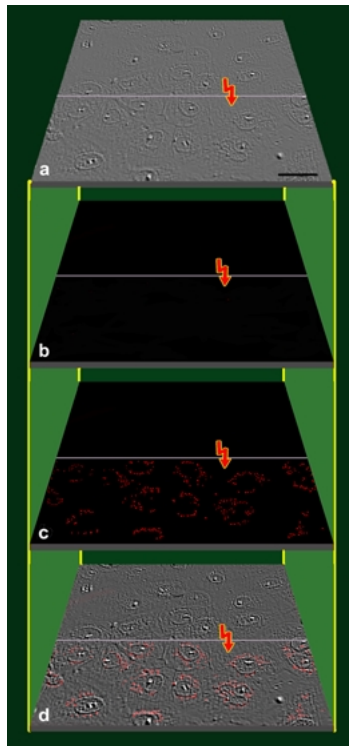
FIGURE 9-2 Detection of generation of ROS in one half of PtK2 cells irradiated with an 800 nm NIR laser at a mean power of 7 mW using a Jenchrom px blue. (*a*) Emboss-filtered transmission image of a monolayer of PtK2 cells before irradiation. (*b*) Autofluorescence image before NIR irradiation. (*c*) NIR femtosecond-laser-induced (at mean power of 25 µW) fluorescence image of the Jenchrom reaction product formed exclusively in one half of the cells exposed to a high laser power (7 mW). (*d*) Electronically merged transmission and fluorescence images, showing the discrete presence of punctate fluorescent products only in high-power (7 mW) NIR-irradiated cells.
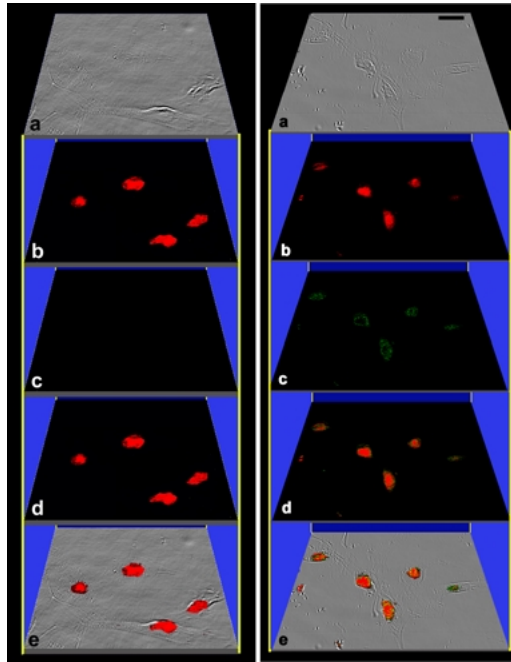
FIGURE 9-4 False-color-coded 3D representation of PtK2 cells exposed to NIR femtosecond laser pulses at a mean power of 2 mW. Two-photon images: (*a*) transmission; (*b*) PI fluorescence; (*c*) TUNEL-negative nuclei, without fluorescein fluorescence; (*d*) electronically merged PI and fluorescein fluorescence; (*e*) overlay of transmission and fluorescence images. The scale bar represents 15 μm.
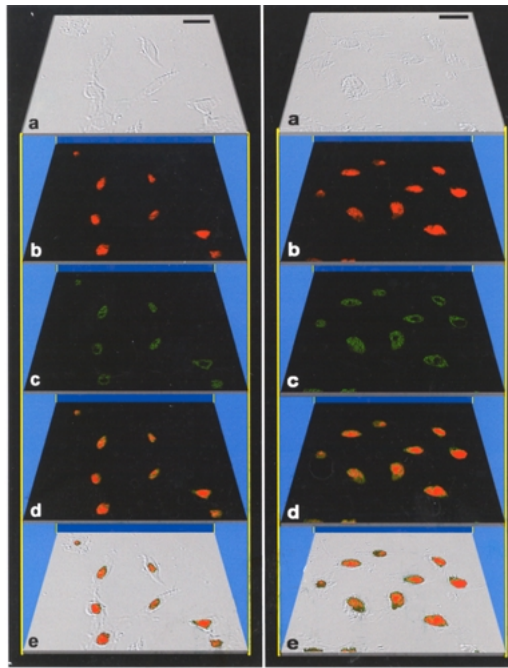
FIGURE 9-5 Pseudocolor-coded 3D representation of PtK2 cells exposed to NIR femtosecond laser pulses at a mean power of 5 mW. Two-photon images: (*a*) transmission; (*b*) PI fluorescence; (*c*) TUNEL-positive nuclei, showing fluorescein fluorescence; (*d*) electronically merged PI and fluorescein fluorescence; (*e*) overlay of transmission and fluorescence images. The scale bar represents 15 μm.
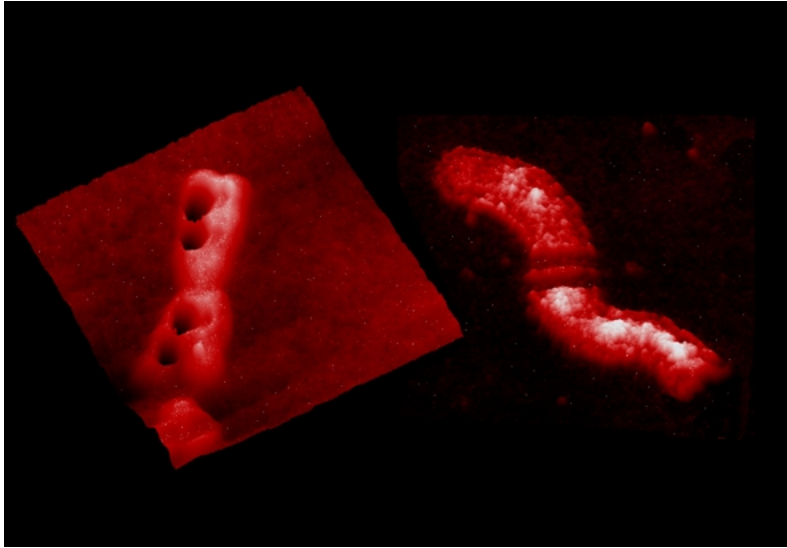
FIGURE 9-7 Nanoprocessing of human chromosomes with 80 MHz NIR femtosecond laser pulses at 800 nm.
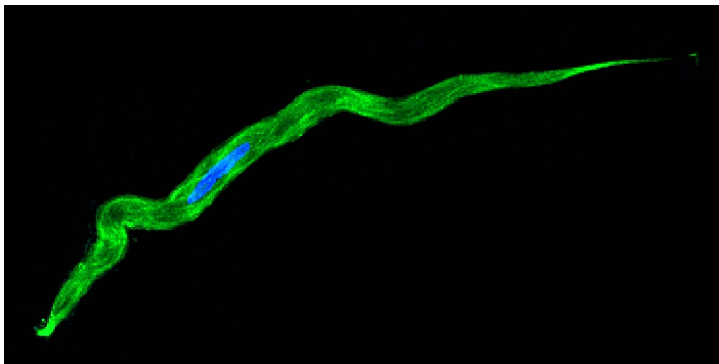

FIGURE 10-5 Dual-labelled smooth muscle cell. DAPI three-photon excitation; Alexa 568 two-photon excitation.
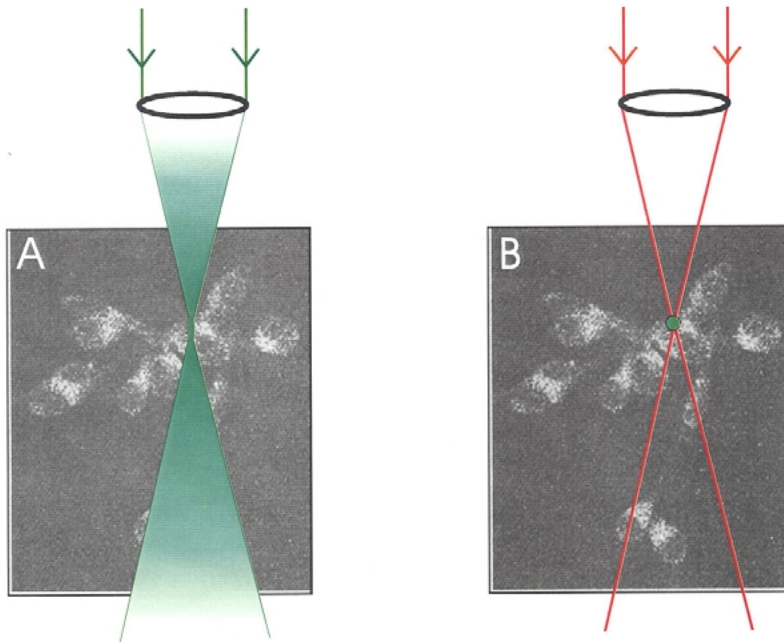
FIGURE 13-1 Illustration of excitation-light path in wide-field epifluorescence or confocal (*A*) microscopy and two-photon excitation microscopy (*B*). In (*A*), the illumination occurs throughout the field of view, whereas in two-photon-excitation fluorescence microscopy, it is limited to a spot at the focal plane of the infrared laser beam.
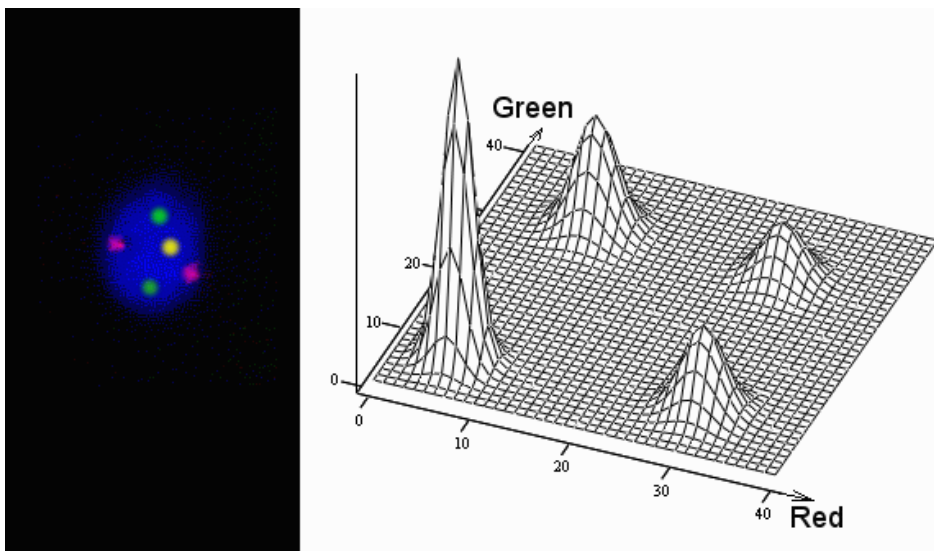

FIGURE 14-4 Use of the two-color histogram (a simulation). The cell at the left has two red and two green dots, and one yellow dot where the red and green fluors overlap. The red-versus-green histogram shows peaks corresponding to background, red dots, green dots, and the yellow dot. The volume under each peak is the total area of the corresponding dots.
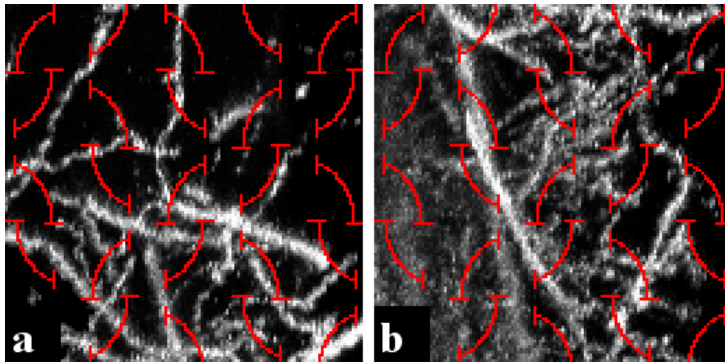
FIGURE 15-3 The method of total vertical projections applied to Golgi-stained nerve cells. (*a*) In this total projection, the cell extensions do not overlap too much, so that it is possible to count intersections between cycloid arcs and cell extensions. (*b*) The cell extensions overlap too much in this projection.
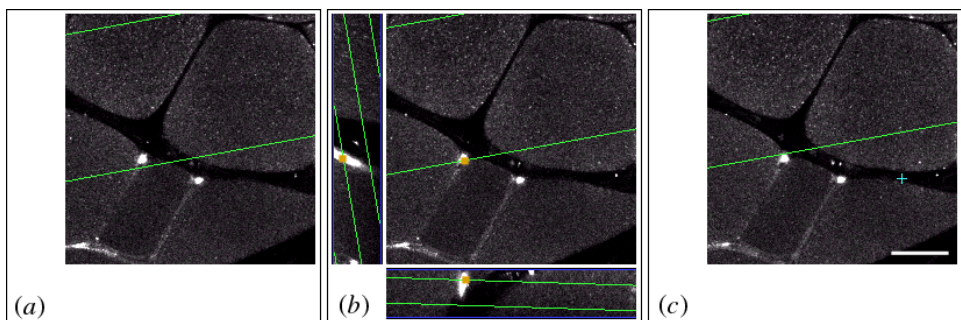

FIGURE 15-6 Estimation of muscle capillary length by the slicer method using the SLICER program. Three successive serial sections of the muscle, 1 μm apart, are shown (*a*), (*b*), and (*c*). Green lines represent the intercepts of the slicer planes with the current section. In the first section (*a*), the slicer plane is going near the capillary profile (bright spot). In the second section (*b*), the slicer plane is intersecting the capillary – the intersection is marked by a yellow point. The orthogonal views of the muscle slice containing the intersection point are shown on the left and bottom side (*b*). In the third section (*c*), the slicer plane is already leaving the capillary profile. The scale bar represents 20 μm. Reproduced by permission from Kubínová and Janáek (2001). Copyright 2001, John Wiley & Sons, Inc.
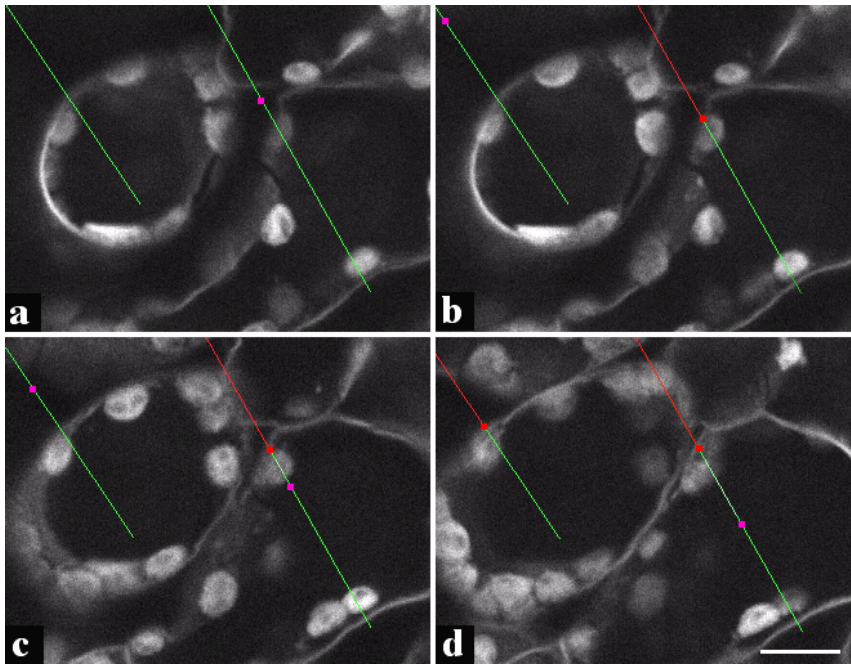
FIGURE 15-14 The fakir method applied to the estimation of the area of exposed surface of mesophyll cells in barley leaf using the FAKIR program. Four serial optical sections 2 μm apart are shown. The test lines of the fakir probe piercing the mesophyll cells are green at the beginning of the measurement (*a*). The violet points denote the intersection points between the test lines and the current section. As soon as such a point comes into contact with the cell wall during focusing-through, it is marked by a mouse as a red point and the part of the test line above this point becomes red (*b*, *d*). The scale bar represents 10 μm.
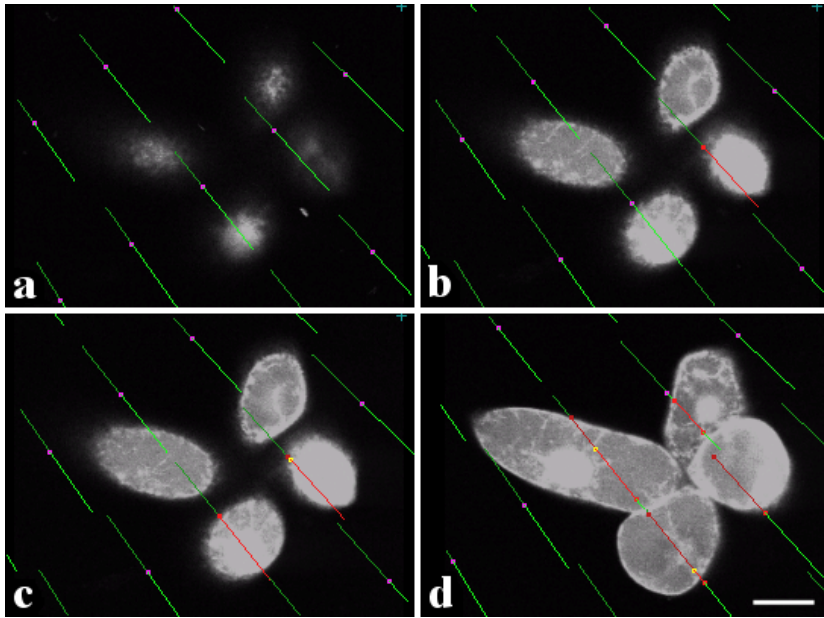
FIGURE 15-20 The fakir method applied to surface-area and volume estimation of a tobacco cell chain using the FAKIR program. The process of marking intersection points between the cell surface and the fakir probe is shown during focusing through the cell chain. Three serial optical sections of the cell chain are shown in (*a*), (*b*), and (*c*). The test lines of the fakir probe piercing the cell chain are green at the beginning of the measurement (*a*). The violet points denote the intersection points between the test lines and the current section. As soon as such a point comes into contact with the cell profile during focusing-through, it is marked by a mouse as a red point and the part of the test line above this point becomes red (*b*). On the red part of the test line, its intersection point with the current section is denoted by a yellow point (*c*). After marking all intersection points, the parts of the Fakir probe lying inside the cell chain are red (*d*). The length of these red intercepts is used for the cell chain volume estimation while the number of red intersection points is proportional to its surface area. The scale bar represents 20 μm. Reproduced by permission from Kubínová and Janáček (2001). Copyright 1999, John Wiley and Sons, Inc.
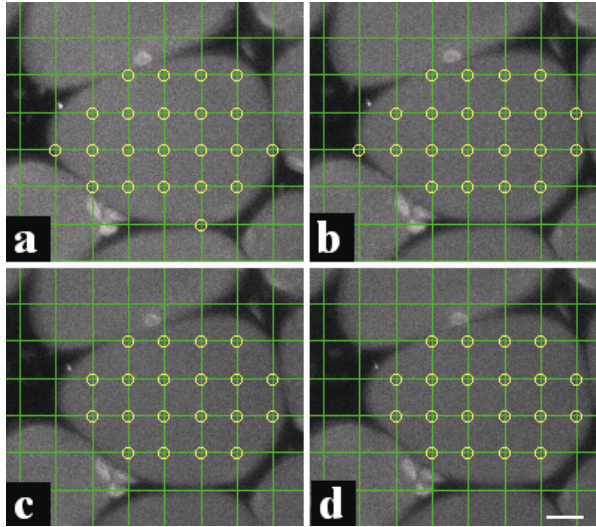
FIGURE 15-22 The method using a cubic spatial grid of points applied to muscle-fiber volume estimation using the SANDAU program. The test points (given by the knot points of the test grid) falling into the fiber within the $40\,\mu m$ thick muscle slice are counted. The grid constant is $10\,\mu m$ here; the estimated volume of the muscle fiber slice is thus equal to $(22 + 21 + 20 + 20)\times 1000\,\mu m^3 = 83\,000\,\mu m^3$.

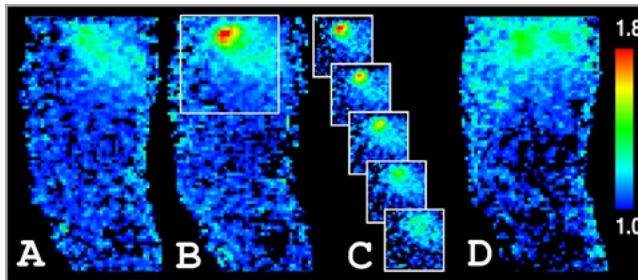**FIGURE 16-1** Three selected pseudocolored 3D images of $[Ca^{2+}]$ in a smooth muscle cell during onset and decay of a calcium spark, reflecting a brief release of $[Ca^{2+}]$ from internal stores of $[Ca^{2+}]$ (Kirber et al., 2001). These are taken from a time series of 32 three-dimensional images. The pseudocoloring gives the ratio of each image to the 3D image at time 0. (*a*) is at time 265 ms; (*b*) is at time 285.5 ms; (*d*) is at time 503.5 ms. In (*a*), (*b*), and (*d*), each image is a projection of five focus planes taken while continuously moving the objective with $1\,\mu m$ of motion during each 2D image. Each 2D image is a 5 ms exposure; each 3D image took 26.5 ms, including focus turnaround time at the top or bottom of each image. Each 3D image is restored, incorporating the motion blur of the continuous motion focus change into the point spread function used in the image restoration. (*c*) is a view of the five separate planes of the image restoration of the spark in (*b*). While the spark appears in the volume projection to be in the center of the cell, the view of the individual planes of the restored spark image in (*b*) shows that it is actually near the bottom of the cell.
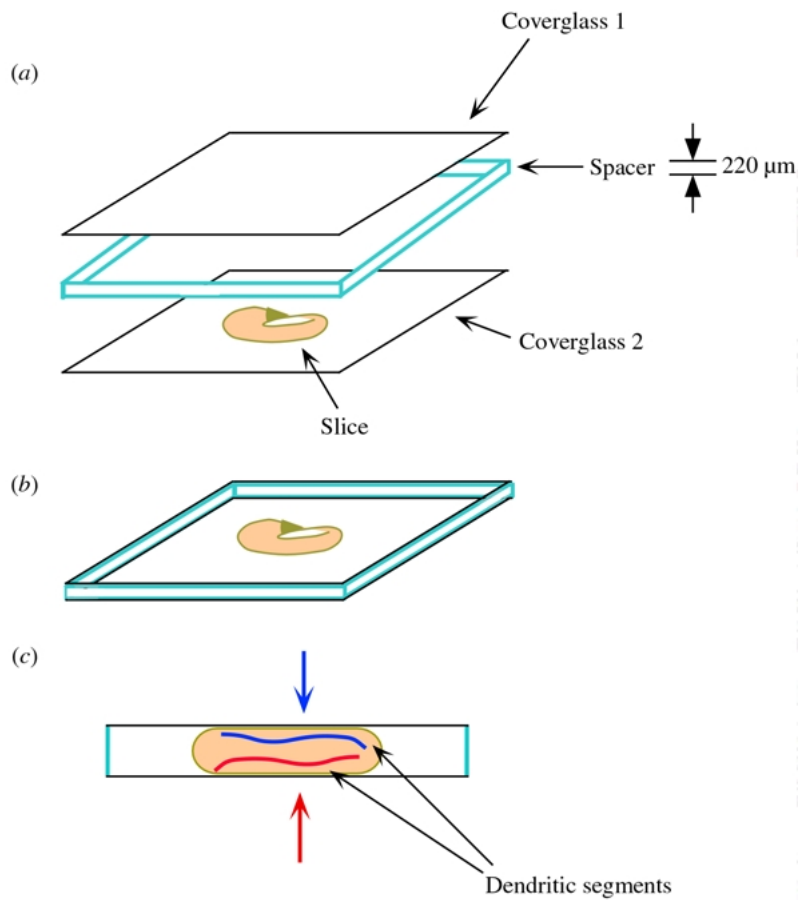
FIGURE 18-1   Fixed slices were embedded in saline, between two coverglasses, in order to allow optical access from both sides. (*a*) The slice was placed at the center of one coverglass, directly on the surface (with as little saline as possible between the slice and the glass). The rectangular spacer was glued directly on the coverglass, and the second coverglass was placed on top. (*b*) Diagrammatic view of the slice embedded between the two coverglasses. (*c*) Side view of the slice, indicating the position of two dendritic segments, at different depths within the slice. The dendrite drawn in red would not be visible from the top side due to the limits of the working distance of the objective and other optical problems (Section 4.1.2). For clarity of the illustration, the thicknesses of the spacer and the coverglass (which in fact are quite similar) are not shown to scale.
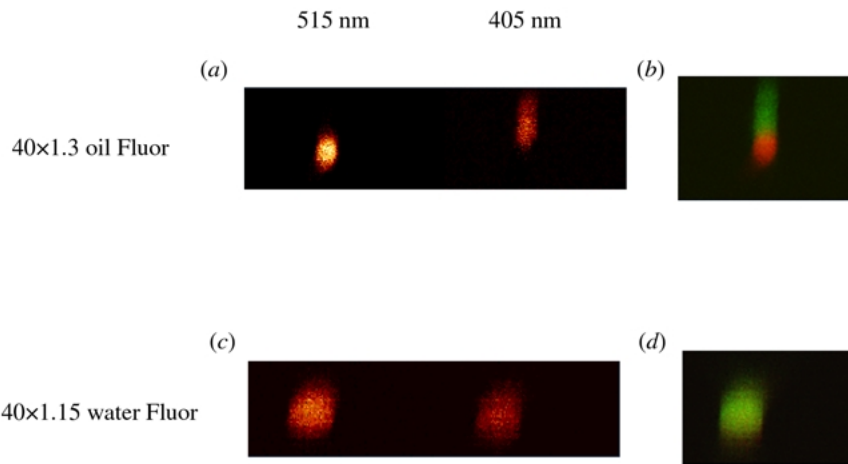
FIGURE 18-2 Illustration of the differences in chromatic correction of the objective lenses indicated. We imaged doubly labeled fluorescent beads, 4 μm in diameter, mounted in water. (*a*) and (*c*) show simultaneously acquired cross-sectional images (viewed along the *x–z* plane) of a single bead, at the emission wavelengths indicated. It can be seen in (*a*) that, because of inadequate color correction, the two fluorescence images, coming from the same bead, do not align along the *z* axis. In contrast, when the same bead is imaged with the other objective, the two images are perfectly aligned (*c*). Such a considerable difference in chromatic performance was unexpected, since both objectives had the same chromatic specification (Fluor). This result indicates that significant differences can exist even between objectives of similar specifications, and therefore individual testing is essential when maximum performance is required. Both objectives also have reduced ultraviolet transmission, since the image obtained at 405 nm is significantly dimmer than that obtained at 515 nm, with the oil objective being slightly brighter. For ease of comparison, the images from (*a*) and (*c*) are shown as green–red overlays in (*b*) and (*d*), respectively. Finally, as can be seen in (*a*), the oil-immersion objective lens has significant spherical aberration, because the beads were mounted in water. Thus, the spherical bead appears elongated along the *z* axis. It is possible to compensate for such distortions, by choosing an immersion oil with a different refractive index (Section 4.1.2). Data for the $40 \times /1.15$ objective lens were acquired with higher zoom, and hence the bead appears bigger. All images appear in pseudocolor.
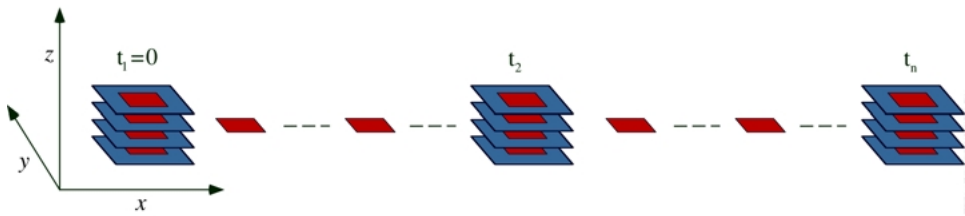
FIGURE 18-3 Paradigm of image acquisition during the time-lapse experiments. A series of optical sections in depth (shown in blue) was acquired at the beginning of the experiment ($t_1 = 0$) to provide the baseline location and morphology of one or a few axons within the region of interest. A maximum-projection image of such a data set is shown in Figure 6. The procedure was repeated at regular intervals ranging between 30 and 60 minutes ($t_2, \ldots, t_n$). In between, high-power (shown in red) single images were acquired at short intervals (60–120 s) to document the changes in morphology and behavior of one or two growth cones within the region of interest. Such data are shown in Figure 7. The difference in size of the blue and red images is meant to reflect the different magnifications (selected by the zoom factor of the confocal).
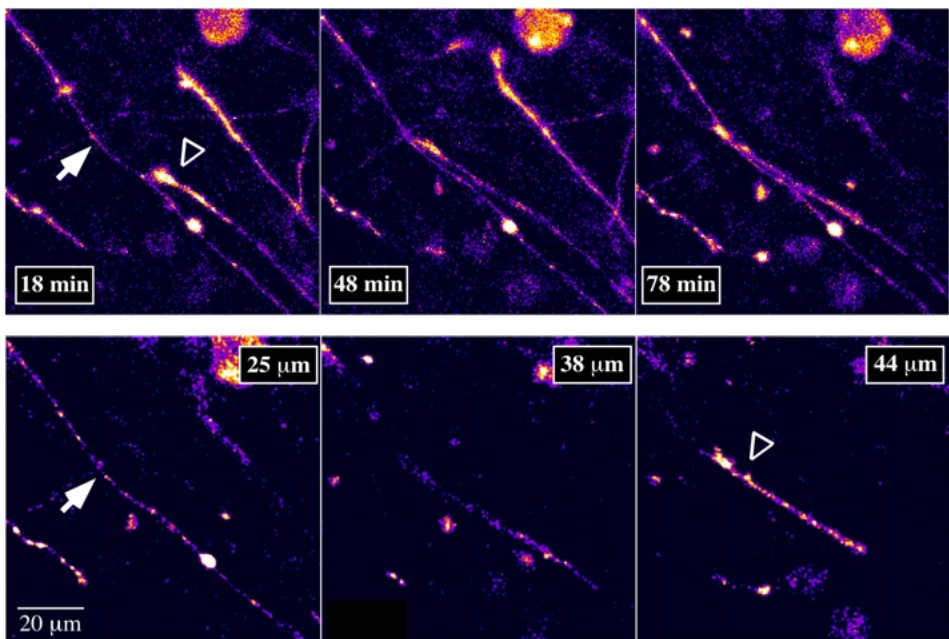

FIGURE 18-4 The panels in the top row are maximum-projection images, generated from a series of confocal optical sections spanning 30 μm in depth and separated by time intervals of 30 minutes. It can be seen that the axon towards the centre (open arrowhead) is extending forward and, in the third top panel, appears to be growing on top of another axon (closed arrow). However, analysis of the single optical sections (bottom row) reveals that the two axons are in fact separated by about 20 μm. Maximum-projection images were created by a "brightest-point algorithm" that performs a pixel-by-pixel comparison of a series of optical sections and uses the brightest point from each one in order to create the projection image. Projection algorithms (using either the brightest point or the average) are an integral part of all 3D image-analysis software packages presently available, as well as some of the image-acquisition software packages that accompany confocal systems.
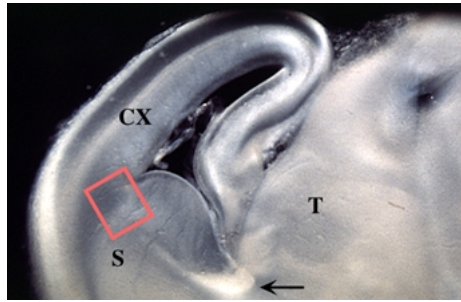
FIGURE 18-5 Photomicrograph of a thalamocortical slice obtained under transillumination. The red box indicates identification of the area of interest to be subsequently imaged. CX, cortex; T, thalamus; S, striatum. The arrow indicates the trajectory of thalamic axons as they exit the thalamus, traverse the striatum, and head towards their cortical targets.
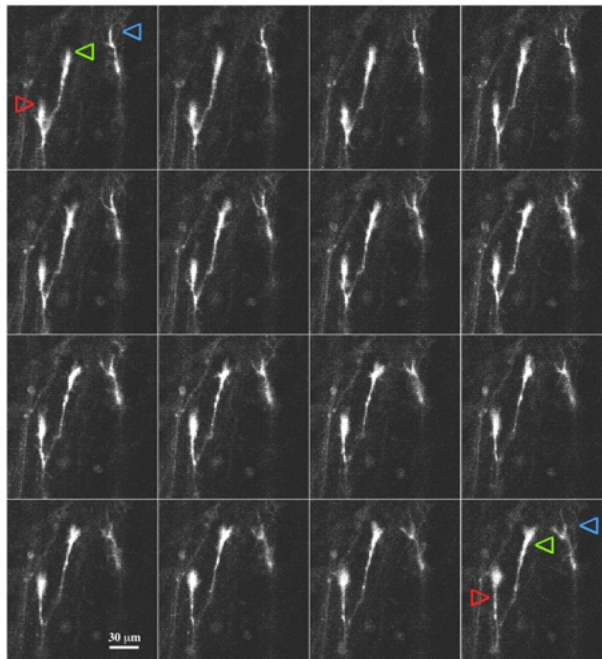

FIGURE 18-7 Time-lapse sequence of three growth cones located at the same focal plane within the region of interest (their relative positions compared with Figure 3 have changed in the 90 minutes since the previous image was acquired). Each panel is a single confocal image collected at 90 s intervals. Arrowheads indicate the position of the leading tip of the axons at the onset of the imaging session. It can be seen that for the duration of the experiment illustrated here, the growth cone at the right-hand corner of each panel does not advance at all (blue arrowhead), whereas the other two move forward by 18 μm (green arrowhead) and 30 μm (red arrowhead), respectively. Interestingly, the first axon, which had been "static" for about 6 hours, later began a vigorous forward extension (Skaliora et al., 2000). An animated version of the static growth cone can be found at http://nucleus.med.upatras.gr/hsn/. Such comparisons are useful because they indicate that the reduction or even the arrest of extension is part of the normal growth process and does not in itself indicate a damaged or unhealthy axon.
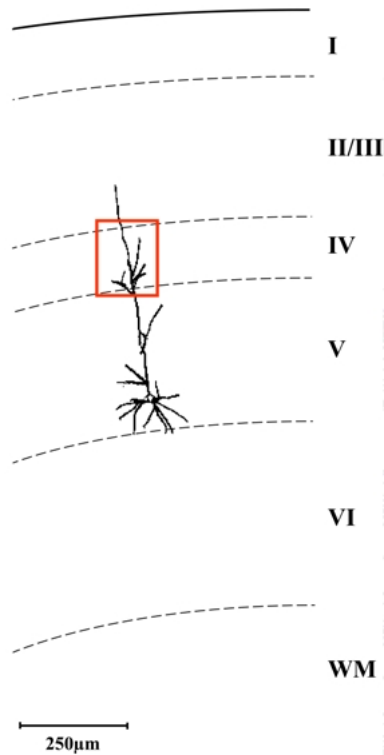
FIGURE 18-9 Digitized version of camera-lucida drawing of a layer 5 pyramidal cell, after it had been scanned on the confocal. Such drawings were made in order to have a complete view of the cells whose dendrites were included in the quantitative analysis. To obtain confocal records of the entire neuron would have been too time-consuming and, at least in this case, irrelevant to the aim of the study. The area within the red box appears in the left panel of Figure 11 as a 3D reconstruction.
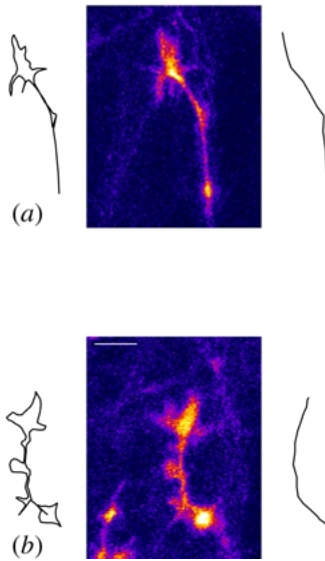
FIGURE 18-10   Examples of types of measurements made for the analysis of axon outgrowth. The pseudocolored images in the middle are single confocal pictures of the distal segment of an axon and its growth cone at different points in time. The black lines on the right of each image illustrate the kind of measurement used to calculate axonal extension: the outline of an axon is followed from a stable measuring point to the most distal tip of the growth cone. The lines on the left of each image illustrate the measurements used to calculate growth cone activity: in this case, all visible side branches and filopodia were incorporated in the measurements. The scale bar represents 10 μm.
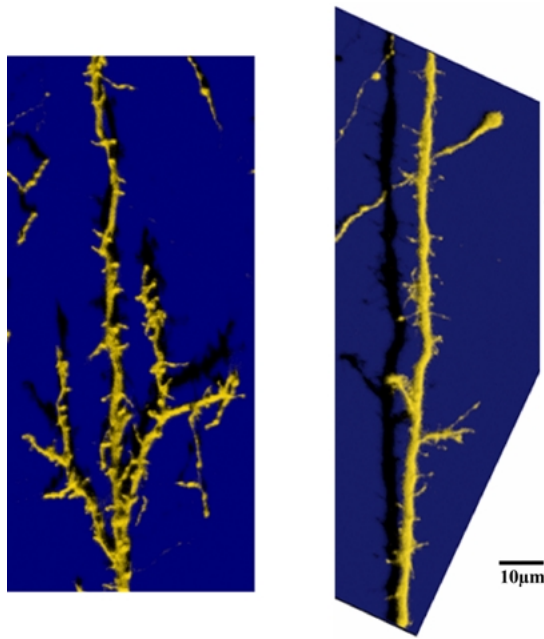
FIGURE 18-11 Three-dimensional visualization of dendritic segments is obtained by combining a series of single confocal images in depth. To create these reconstructions, the visualization method "Simulated Fluorescent Process" of the Imaris software (see Section 3.3) was used. In short, each voxel of the 3D dataset is assigned an absorption and an emission factor based on its intensity in the original dataset. This information, together with the depth information, is used to assign the transparency and the shadow-casting properties of the final image (Messerli et al., 1993).
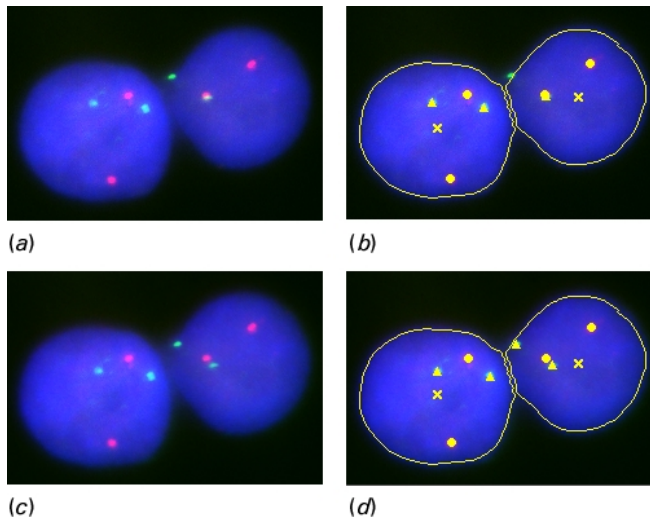
FIGURE 19-3 Example of chromatic-aberration correction. Study of the topology of the genes *ABL* (green) and *BCR* (red) in human cell nuclei (blue). The genes are visualized using the FISH technique. Image data (*a*, *c*) and analysis results overlaid over the image data (*b*, *d*) are shown. Uncorrected images (*a*, *b*) are compared with the images corrected for chromatic aberration (*c*, *d*). Only part of the whole image is shown. The nuclei are about 10 μm in diameter. The analysis results are visualized in yellow: the *ABL* genes are shown as triangles, the *BCR* genes as circles, and the nuclear boundaries as closed curves. Note that one of the *ABL* genes is out of the nucleus before correction, whereas after correction it gets into the correct place. Consequently, this gene was rejected from the analysis without correction, whereas after correction it was safely detected. Note also that the *ABL* and *BCR* genes coincide in the right nucleus before correction, but are well separated after correction. This means that, without correction, the right nucleus is wrongly classified as Philadelphia (Ph)-positive (carrying the t(9;22) translocation), whereas after correction it is correctly classified as Ph-negative (no t(9;22) translocation present). Reprinted from Kozubek and Matula (2000).
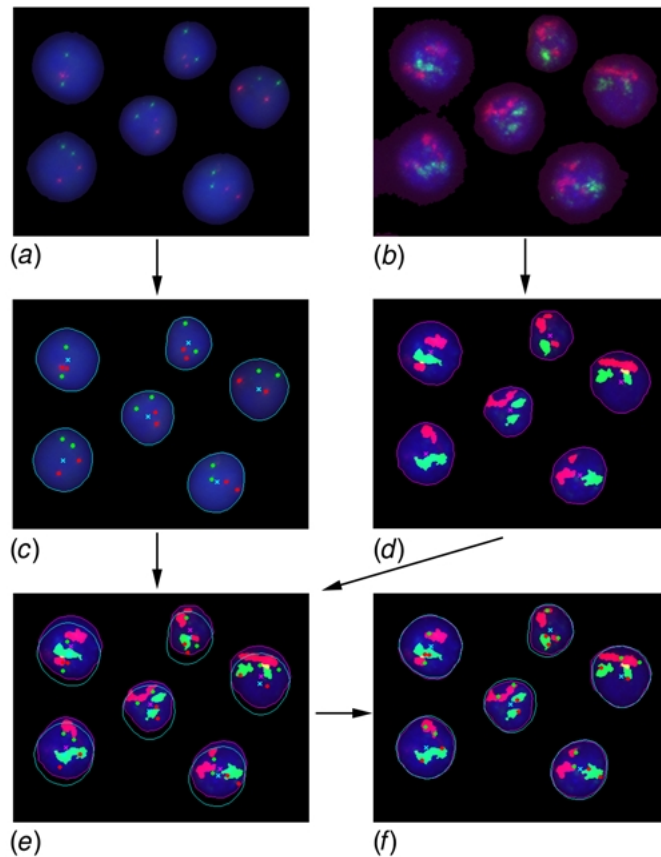
FIGURE 19-5 Merging of results from two different hybridizations of the same microscope slide. In the first hybridization (*a*), the *ABL* gene was stained with FITC (green), the *BCR* gene was stained with rhodamine (red), the counterstain was DAPI (blue), and the image was acquired in wide-field mode. In the second hybridization (*b*), the territory of chromosome 9 was stained with rhodamine (red), the territory of chromosome 22 was stained with FITC (green), the counterstain was DAPI (blue), and the image was acquired in confocal mode. Only a part of the whole field of view is shown (about 60 μm×45 μm) for both hybridizations in so-called autofocus (maximum-projection) mode. Each hybridization was analyzed separately. The results of the analysis are visualized using small circles for genes (*c*) and territory highlighting for chromosomes (*d*). The visualization color was set identical to the original emission color of the genetic loci. The nuclear boundaries (closed curves) and weight centers (crosses) are highlighted in cyan (first hybridization) and magenta (second hybridization). The two independent analysis results were subsequently overlaid (*e*), and corresponding pairs of nuclei were determined. Because of microscope-stage imprecision, the positions of nuclear weight centers do not match – they are shifted by a certain vector. After the determination of this vector, the nuclei can be correctly overlaid (*f*), enabling visualization of the gene positions within chromosome territories. Reprinted from Kozubek M. et al. (2001).
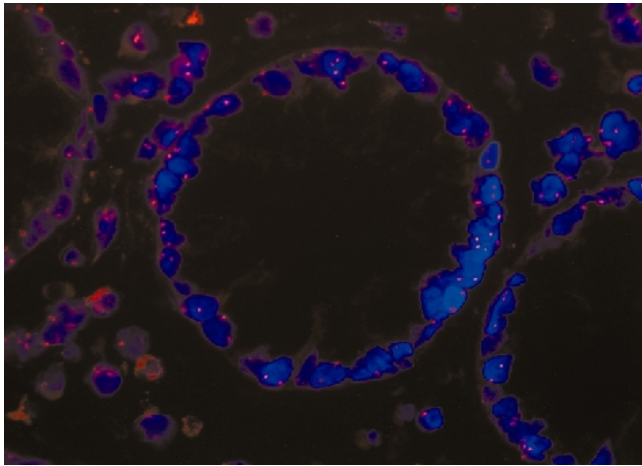
FIGURE 19-6 Typical example of a maximum-projection image of 3D fixed 4 μm thick colon tissue section with FISH signals of the chromosome 7 centromere. The nuclei were counterstained with DAPI. Reprinted from Koutna et al. (2000).
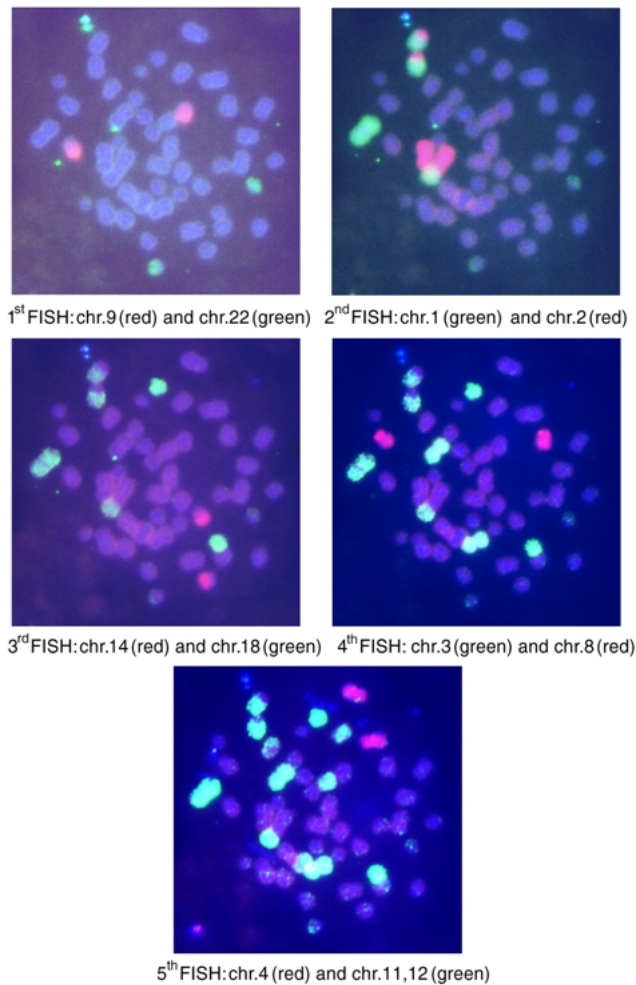
1st FISH: chr.9 (red) and chr.22 (green)   2nd FISH: chr.1 (green) and chr.2 (red)

3rd FISH: chr.14 (red) and chr.18 (green)   4th FISH: chr.3 (green) and chr.8 (red)

5th FISH: chr.4 (red) and chr.11,12 (green)

FIGURE 19-7 Repeated FISH on metaphase spreads: chromosomal aberration scoring after irradiation. Human lymphocytes were irradiated with fast neutrons from the d→Be reaction with a dose of 1.5 Gy and were repeatedly stained by FISH. Chromosome-specific probes were purchased from Cambio and Oncor. Biotin-labeled probes were stained with FITC (green) and digoxigenin-labeled probes were stained with rhodamine (red). The counterstain was DAPI (blue). The same mitosis is shown for five subsequent hybridizations. Note that whereas digoxigenin (red) can be washed out without problems, biotin (green) remains on the chromosomes also in the next staining. In the second hybridization, a dicentric between chromosomes 1 and 2 with two common acentric fragments is clearly visible.
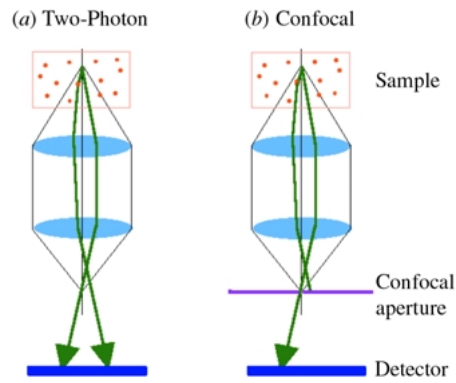
FIGURE 20-1 The effect of a confocal pinhole aperture on photon-collection efficiency in the presence of a strongly scattering specimen. (*a*) In the two-photon case, there is no pinhole and the large detector collects both deflected and undeflected photons. (*b*) In the confocal case, the deflected photons are blocked by the pinhole.
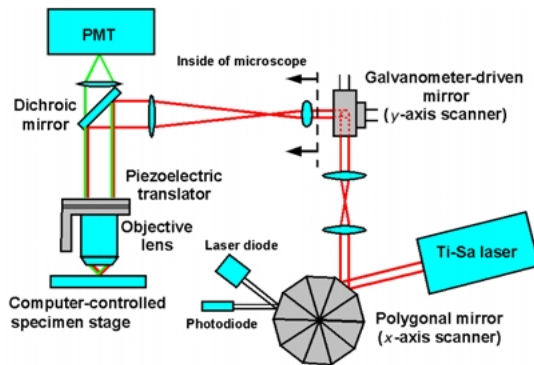

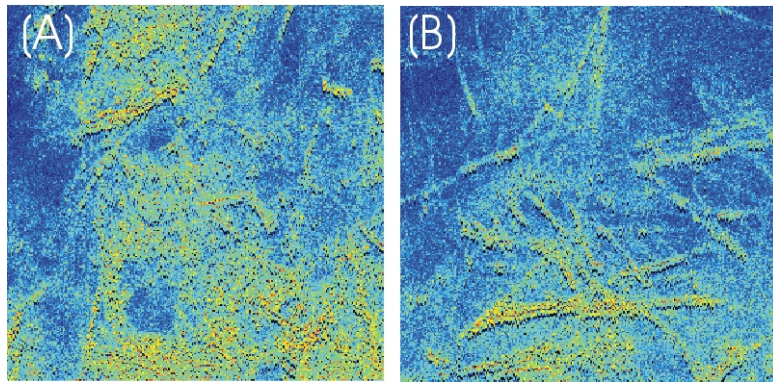**FIGURE 20-4** The schematics of a video-rate two-photon microscope based on a polygonal scanner.

FIGURE 20-5 Video-rate images of collagen/elastin fibers in ex vivo human skin. (*a*) Image acquired at a depth of 60 μm. (*b*) Image acquired at a depth of 120 μm at the same location as (*a*).
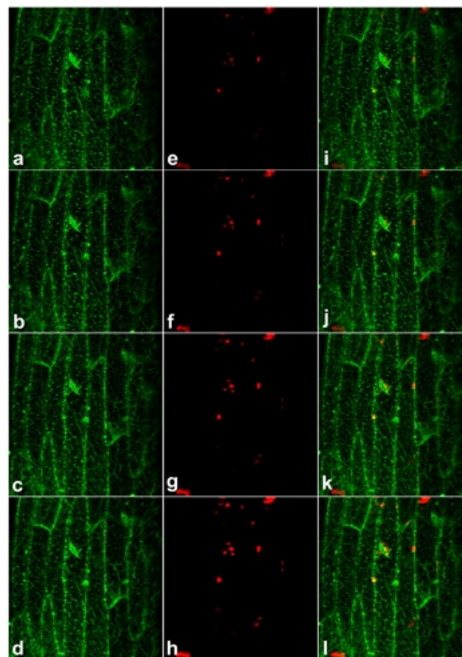

FIGURE 21-7 Simultaneous detection of ER-targeted GFP and autofluorescence of chloroplasts in the cortical region of the hypocotyl of *Arabidopsis* with two-photon femtosecond NIR excitation at 800 nm. (*a*)–(*d*) are serial optical sections (obtained at intervals of 0.25 μm) of the cortical ER, while (*e*)–(*h*) are the corresponding serial sections showing chlorophyll autofluorescence associated with the chloroplasts. (*i*)–(*l*) are electronically merged images of corresponding GFP and chlorophyll fluorescence. Note the distinct presence/association of chloroplasts in the vicinity of the nucleus (arrows), and the reticulate organisation of the cortical ER. The bright green spots associated with the lateral walls correspond to the plasmodesmatal regions.
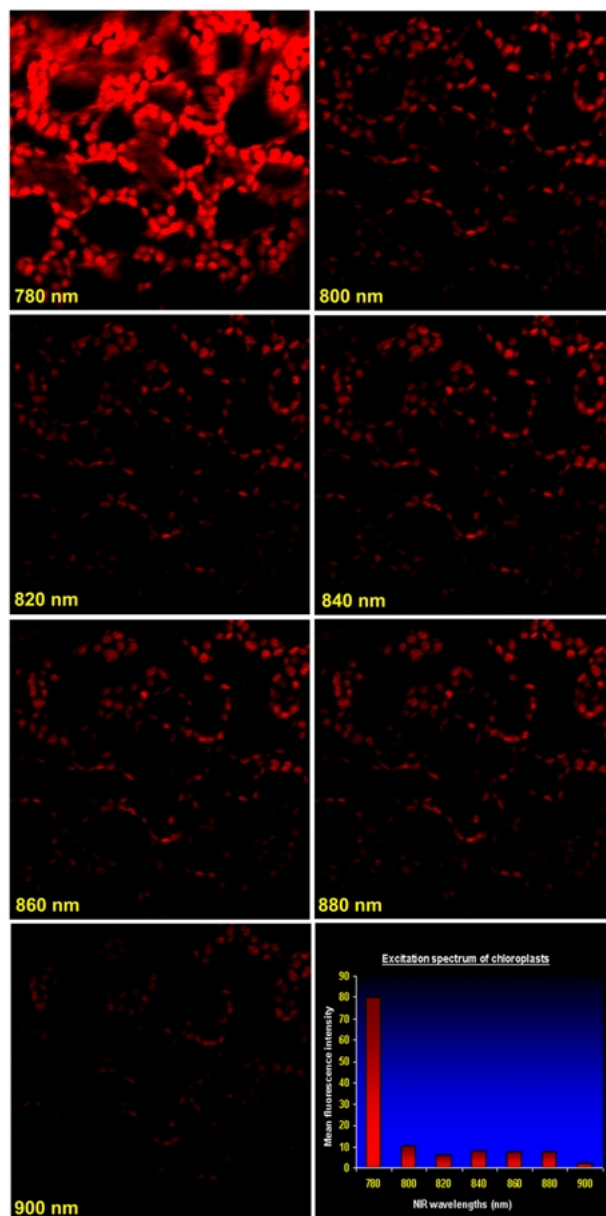
FIGURE 21-11 Two-photon imaging of chlorophyll fluorescence in mesophyll cells following excitation with different NIR wavelengths at 780, 800, 820, 840, 880, and 900 nm. As depicted in the spectrum.
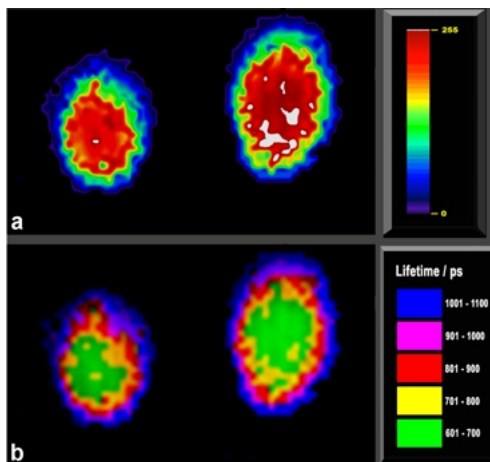
FIGURE 21-12   Two-photon fluorescence intensity (*a*) and τ-image (*b*) of chloroplasts.
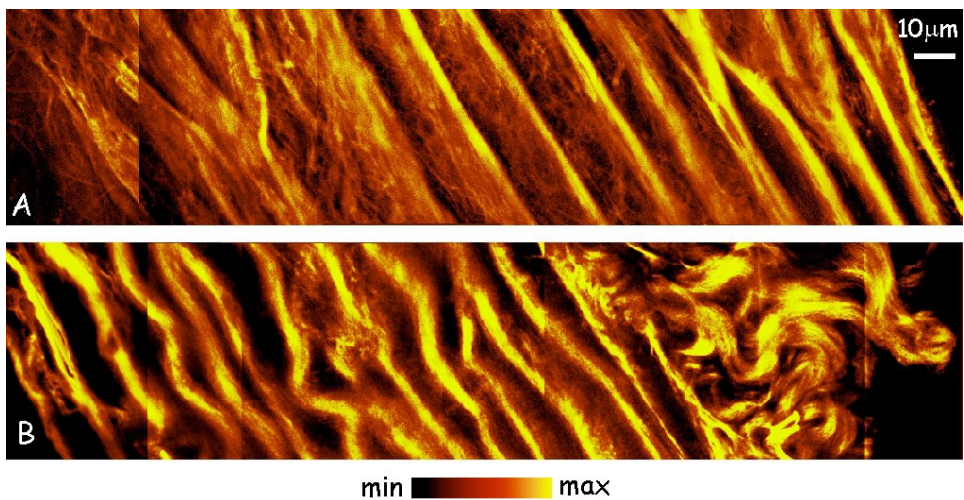

FIGURE 22-1   Pseudocolor representation of a composite image of several adjacent frames of deep optical sections showing the autofluorescence intensity of the matrix fibers: (*A*) in a control sample of a rat aorta cross-section ring from the lumen (right) to the ring exterior (left); (*B*) following treatment with minimally oxidized LDL.
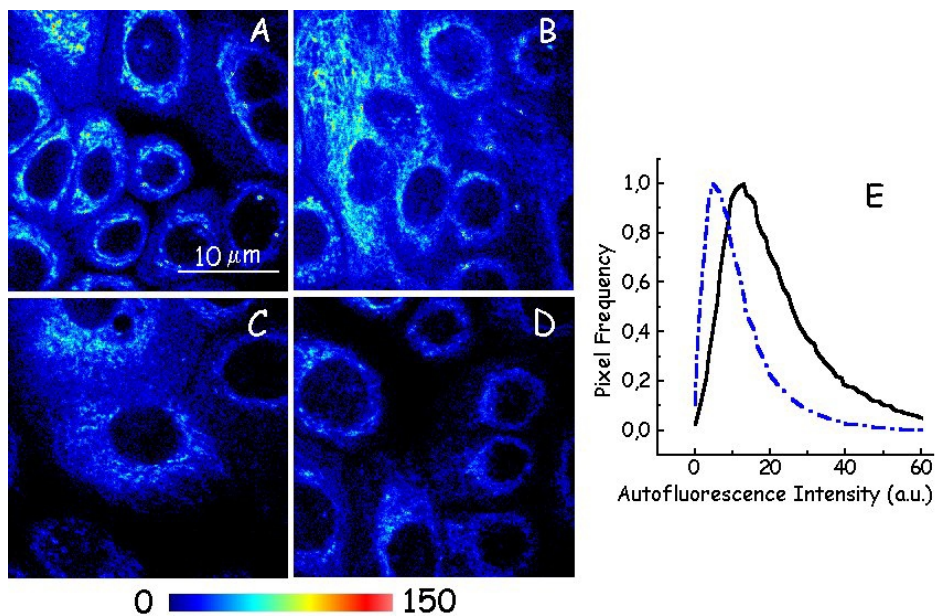
FIGURE 22-4   Pseudocolor representation of the autofluorescence intensity in normal human epidermal keratinocytes. The cells imaged in (*A*) and (*B*) were grown for two days after supplementation with 2 mM NAC. (*E*) Normalized histograms of the autofluorescence intensity for control samples (blue dashed line) and for NAC-treated samples (black continuous line). Each histogram represents the average intensity of four different images.
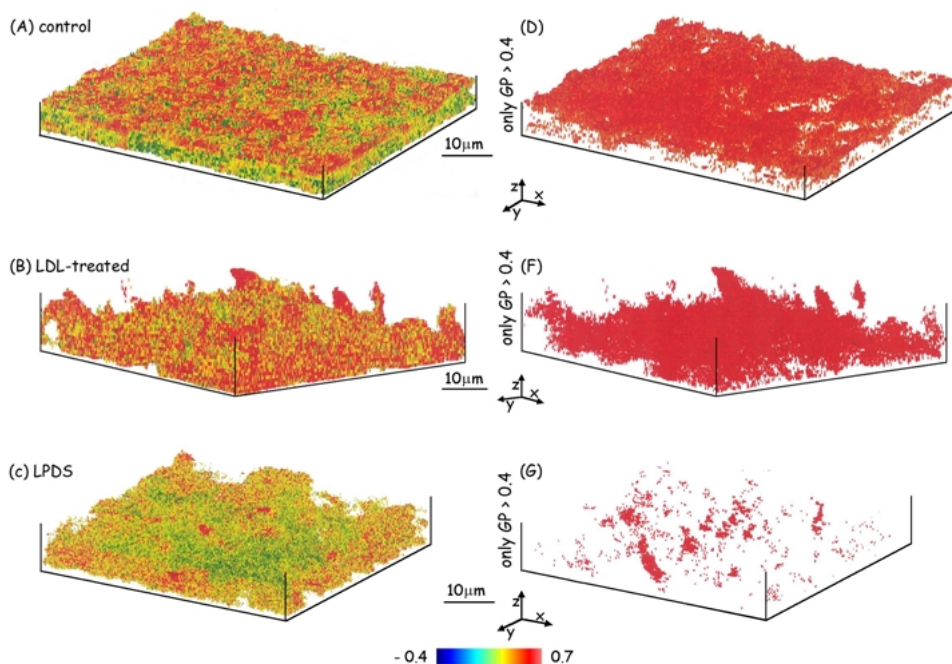
FIGURE 22-6 Three-dimensional pseudocolor reconstruction of Laurdan GP values in membranes of OK cell layers. (*A*), (*C*), (*E*) are obtained from a confluent monolayer of OK cells in control, cholesterol-enriched (LDL-treated), and cholesterol-depleted (LPDS) conditions, respectively. (*B*), (*D*), and (*F*) display the same cell monolayers, viewed as GP values above 0.4 only. Cholesterol enrichment causes a significant increase in GP, with most GP > 0.4, while cholesterol depletion causes a marked decrease in GP, with most of GP < 0.4.
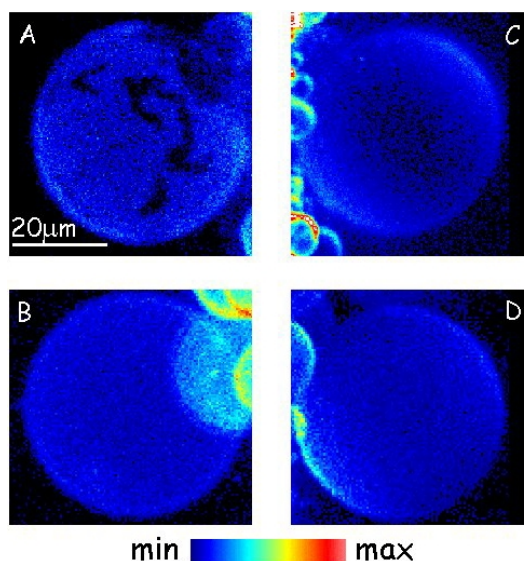

FIGURE 22-7 Two-photon excitation fluorescence microscopy images of GUVs, labeled with Prodan, composed of an equimolar mixture of dilauroyl- and dipalmitoyl-phosphatidylcholine in the absence (*A*, *B*) and presence (*C*, *D*) of 30 mol% cholesterol.